www.nature.com/cr
www.cell-research.com

Cell Research

ARTICLE

Structure of the receptor-activated human TRPC6 and TRPC3 ion channels

Qinglin Tang[1], Wenjun Guo[1], Li Zheng[2], Jing-Xiang Wu[1,3], Meng Liu[2], Xindi Zhou[2], Xiaolin Zhang[2] and Lei Chen[1,3]

TRPC6 and TRPC3 are receptor-activated nonselective cation channels that belong to the family of canonical transient receptor potential (TRPC) channels. They are activated by diacylglycerol, a lipid second messenger. TRPC6 and TRPC3 are involved in many physiological processes and implicated in human genetic diseases. Here we present the structure of human TRPC6 homotetramer in complex with a newly identified high-affinity inhibitor BTDM solved by single-particle cryo-electron microscopy to 3.8 Å resolution. We also present the structure of human TRPC3 at 4.4 Å resolution. These structures show two-layer architectures in which the bell-shaped cytosolic layer holds the transmembrane layer. Extensive inter-subunit interactions of cytosolic domains, including the N-terminal ankyrin repeats and the C-terminal coiled-coil, contribute to the tetramer assembly. The high-affinity inhibitor BTDM wedges between the S5-S6 pore domain and voltage sensor-like domain to inhibit channel opening. Our structures uncover the molecular architecture of TRPC channels and provide a structural basis for understanding the mechanism of these channels.

Cell Research (2018) 28:746–755; https://doi.org/10.1038/s41422-018-0038-2

INTRODUCTION

Studies on *Drosophila melanogaster* light-sensing mutants reveal that the activation of rhodopsin by light results in currents mediated by the transient receptor potential (TRP) channel.[1, 2] Later, a few TRP channel families were identified in other species including mammals. These channels share sequence homology with the founding member Drosophila TRP channel and respond to various stimuli.[3] Based on their primary sequences and activation mechanisms, human TRPC3, TRPC6, and TRPC7 cluster on the phylogenic tree and constitute a receptor-activated TRPC subfamily. Similar to the Drosophila TRP channel, they are non-selective cation channels that are directly activated by diacylglycerol (DAG) produced by receptor-coupled phospholipase C.[4–6] Activation of these channels results in the depolarization of cell membrane and calcium influx. TRPC3/6/7 can form either homotetramers or heterotetramers with variable calcium ion permeability.[7] Based on their sequence features, these channels have a tetrameric transmembrane pore formed by six transmembrane helices, like other TRP channels. In addition, they have a large cytoplasmic N-terminus that contains four ankyrin repeats and a C-terminal coiled-coil motif. How these structural elements are assembled into the tetrameric TRPC channel is largely unknown.

TRPC3/6/7 are broadly distributed in human tissues and involved in many physiological or pathological processes, such as synaptic formation,[8] motor coordination,[9] kidney function,[10, 11] wound healing,[12] cancer progression,[13] smooth muscle contraction,[14] and cardiac hypertrophy induction.[15] Notably, TRPC6 is important for kidney podocytes foot processes and genetic mutations in human TRPC6 can cause familial focal segmental glomerulosclerosis (FSGS),[10, 11, 16–18] a kidney disease manifested by proteinuria.[19]

Despite the physiological importance of receptor-activated TRPC channels, their architecture and mechanism remain elusive due to a lack of high-resolution structures. To gain insights into the mechanism of receptor-activated TRPC channels, we embarked on the structural study of human TRPC6 and TRPC3 channels and determined their structures in lipid nanodiscs. The structures reveal a new architecture of the TRP channel family. Together with functional data, we also elucidated the structural basis of high-affinity binding by a novel inhibitor.

RESULTS

Discovery of a high-affinity inhibitor for hTRPC6

Gain-of-function mutations in human TRPC6 can lead to excessive calcium influx in kidney podocytes and familial FSGS.[20] Currently, it is a clinical challenge to effectively cure this disease,[19, 21–23] and patients can easily develop end-stage renal disease, which can only be treated by frequent renal dialysis or kidney transplant. Pharmacological inhibition of TRPC6 is a promising way to alleviate clinical symptoms in FSGS patients with TRPC6 gain-of-function mutations. Therefore, we screened small molecules that could inhibit hTRPC6-mediated membrane depolarization as lead compounds for the clinical treatment of FSGS. Through this screening, we identified (2-(benzo[d][1,3]dioxol-5-ylamino)thiazol-4-yl)((3 S,5 R)-3,5-dimethylpiperidin-1-yl)methanone (abbreviated, BTDM) as a high-affinity inhibitor for the hTRPC6 channel (Fig. 1a and Supplementary information, Figure S1a and b). We used 1-oleoyl-2-acetyl-sn-glycerol (OAG), a soluble DAG analog to activate

[1]State Key Laboratory of Membrane Biology, Institute of Molecular Medicine, Beijing Key Laboratory of Cardiometabolic Molecular Medicine, Peking University, 100871 Beijing, China; [2]Dizal Pharmaceutical Company, Jiangsu, China and [3]Peking-Tsinghua Center for Life Sciences, Peking University, 100871 Beijing, China
Correspondence: Xiaolin Zhang (Xiaolin.Zhang@dizalpharma.com) or Lei Chen (chenlei2016@pku.edu.cn)
These authors contributed equally: Qinglin Tang, Wenjun Guo.

Received: 22 February 2018 Revised: 22 March 2018 Accepted: 2 April 2018
Published online: 26 April 2018

© IBCB, SIBS, CAS 2018

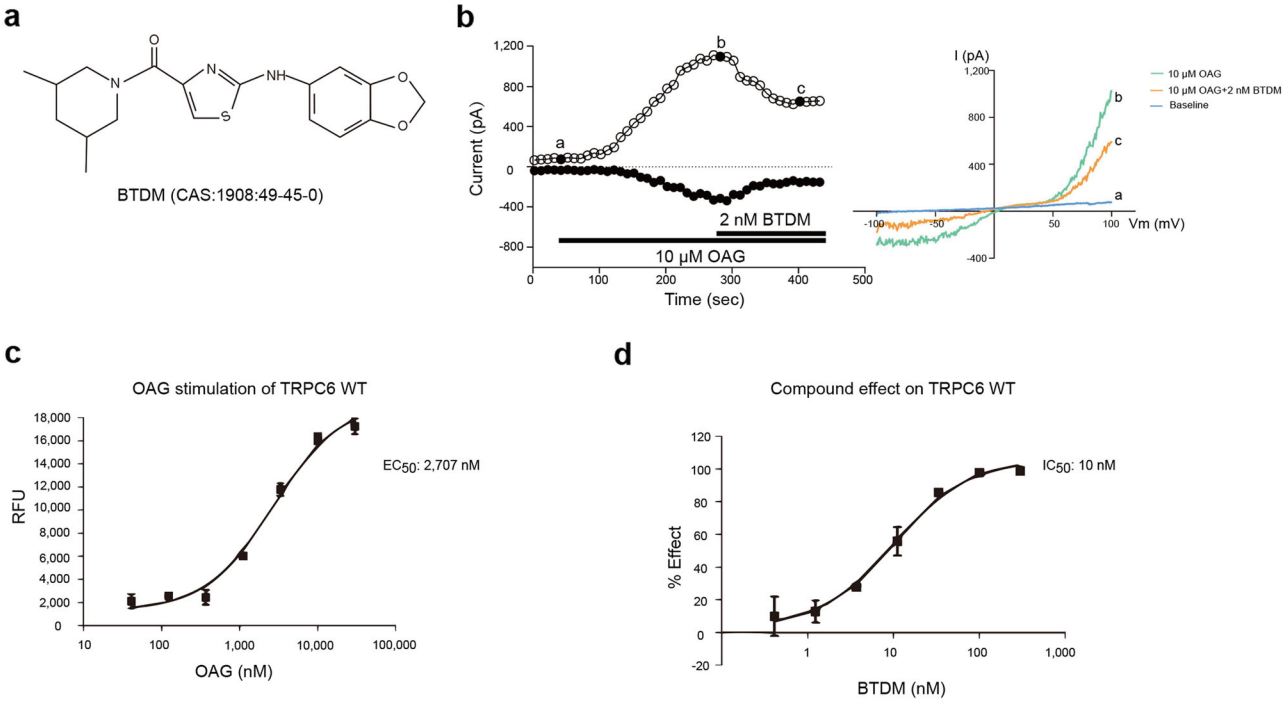

Fig. 1 Characterization of the high-affinity inhibitor BTDM. **a** Chemical structure of the BTDM used in this study. **b** Whole-cell currents of hTRPC6 evoked by OAG were inhibited by BTDM in sub-IC50 concentration. Voltage ramps were applied every 10 s, and the outward current at +100 mV and inward current at −100 mV during each ramp are plotted as a function of time after rupture of the patch for whole-cell recording. Solid and hollow circles represent currents at −100 mV and +100 mV, respectively. Solution exchanges were indicated by horizontal bars. *I–V* curves were obtained during voltage ramps at the time points indicated. The inhibitor could inhibit hTRPC6 currents with the inhibition rate of 45.54% ± 2.22% at 2 nM ($n = 3$). **c** Activation effect of OAG on hTRPC6 constructs, measured by FLIPR membrane potential assay ($n = 3$). **d** Inhibition effect of the BTDM on wild-type hTRPC6 ($n = 3$)

hTRPC6 channel. We found that BTDM potently inhibited OAG-evoked currents and membrane depolarization of cells transfected with hTRPC6 (Fig. 1b–d). In addition, BTDM could suppress the activity of gain-of-function hTRPC6 channel mutants, including P112Q,[11] R895C, and E897K,[10] with similar potency as the wild-type channel (Supplementary information, Table S1), further emphasizing the potential of BTDM as a lead compound. BTDM is also potent against hTRPC3 channel currents evoked by OAG (Supplementary information, Figure S1c-e).

Architecture of the hTRPC6 channel

To stabilize the hTRPC6 channel in closed state, we conducted cryo-electron microscopic (cryo-EM) studies of hTRPC6 in complex with the inhibitor BTDM. The hTRPC6 protein overexpressed in mammalian cells was purified in detergent micelles and reconstituted into nanodiscs for single-particle analysis (Supplementary information, Figures S1f and g and S2). The 3.8 Å cryo-EM map was of sufficient quality for us to model 670 out of the 931 residues (Supplementary information, Figures S3 and S4 and Table S2). The remaining residues were mostly disordered, probably due to their flexibility in the closed state. The hTRPC6 channel tetramer occupies $75 \times 75 \times 150$ Å^3 in three−dimensional space (Fig. 2 and Supplementary information, Video S1). Four protomers pack symmetrically to generate a two-layer architecture: the intracellular cytoplasmic domain (ICD) layer, and the transmembrane domain (TMD) layer (Fig. 2b, c). The central four-fold rotation axis is perpendicular to both layers. The hTRPC6 ICD has an inverted bell shape and caps below the ion channel pore of TMD. Its N-terminus (1–84) was unresolved in our cryo-EM density map. Truncation of the N-terminal amino acids 1–71 did not affect the tetramer assembly or OAG-induced depolarization of membrane potential (Supplementary information, Figure S5 and Table S1), indicating that the flexible N terminal 71 residues were dispensable for hTRPC6 assembly and gating. Four ankyrin repeats (ARs, residues: 96–243) and adjacent linker helices (LHs, residues: 256–393) form the major building block of ICD (Fig. 3). The last three LHs pack against the TRP helix, providing the major contact site between the ICD and TMD (Fig. 3b, c). Immediately after the TRP helix, the TRP re-entrant dips halfway into the phospholipid bilayer (Fig. 3b, c). The amino acids of the cytoplasmic C-terminus of TRPC6 fold into two long helices, namely, C-terminal helix 1 (CH1) and C-terminal helix 2 (CH2). CH1 runs horizontally from the periphery into the center of the channel and connects to the vertical CH2 coiled-coil via a 90° turn (Fig. 3). The amino acids between the TRP re-entrant and CH1 (766–854) are disordered. These residues contain putative binding sites for inositol hexaphosphate (IP_6) (842–868),[24] and calmodulin and IP_3 receptor, namely, the calmodulin/IP_3 receptor binding region (838–872).[24–26] It is reported that calmodulin and IP3 receptor can bind to ICD of TRPC channels to modulate their activity.[24–26]

Inter-subunit interactions mediate hTRPC6 tetramer assembly

Both the ICD and TMD contribute to the tetrameric assembly of the hTRPC6 channel. The ICD of each subunit extensively interacts with the neighboring subunits, forming an inter-subunit interface with the area of 5,483 Å^2 between adjacent subunits (Fig. 4). Specifically, the amino acids of the N-terminal loop (85–94) interact with the LHs of the neighboring subunit (Fig. 4d). The LHs also interact with adjacent LHs (Fig. 4e). Similar interactions were previously mapped biochemically in TRPC4, in which N-terminal 1–304 residues interact with both residues 87–172 and residues 254–304.[27] Moreover, CH1 inserts into the cavity between two neighboring subunits and glues them together (Fig. 4f, h). CH2 helices form a vertical four-helix bundle that further tightens the tetramer (Fig. 4g), reminiscent of TRPA1 and TRPM C-terminal four-helix bundle structures.[28–32] Uniquely, the four CH1–CH2

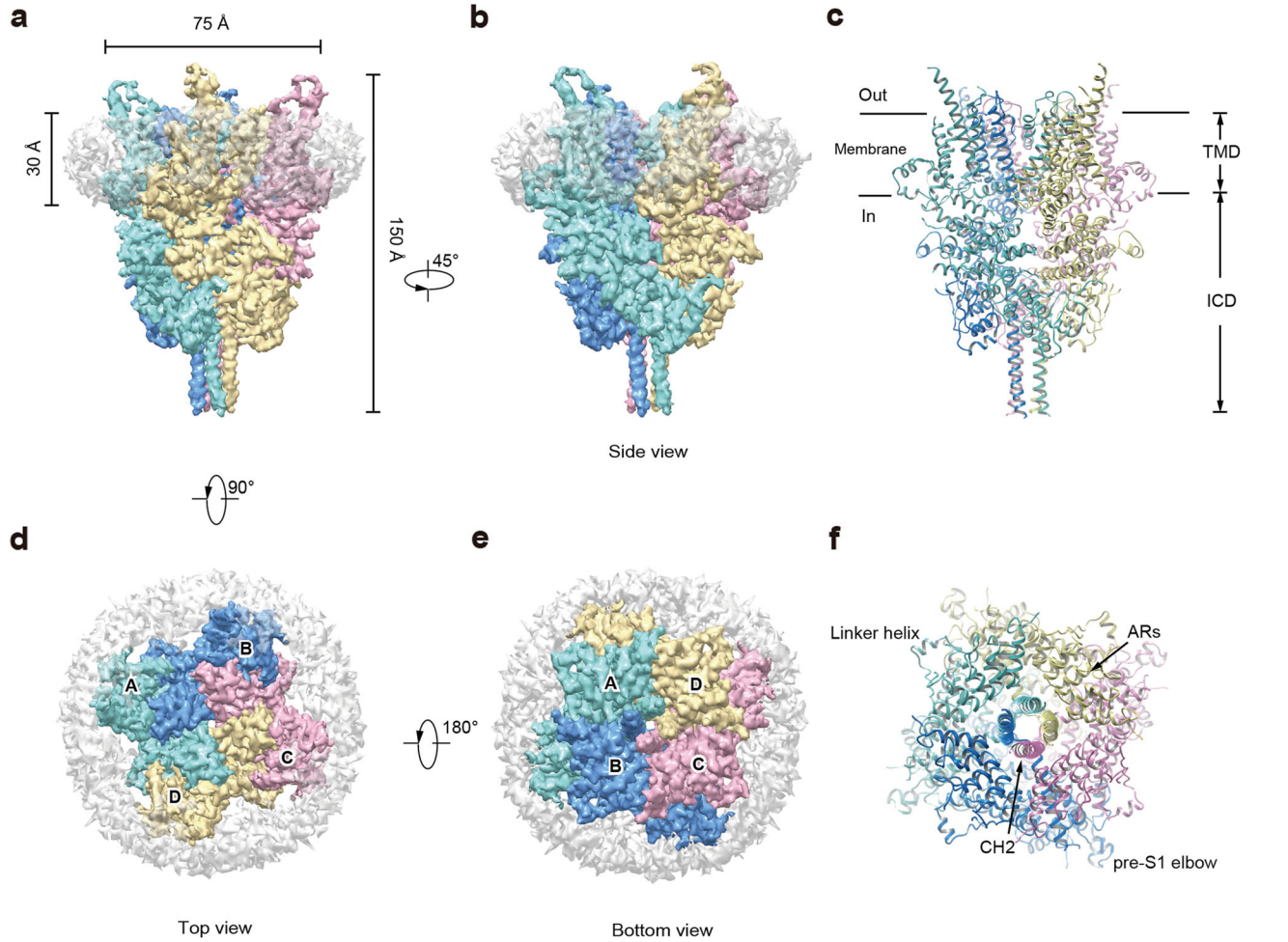

Fig. 2 Cryo-EM density map of the human TRPC6 channel. **a**, **b** Cryo-EM map of hTRPC6 channel is shown in side view. Subunits A, B, C, and D are colored in cyan, blue, pink, and yellow, respectively. Density corresponding to nanodisc is in gray with transparency. **c** hTRPC6 model is shown in cartoon from side view. **d**, **e** Top view (**d**) and bottom view (**e**) of the hTRPC6 channel density map. **f** Bottom view of hTRPC6 model. AR ankyrin repeat, CH C-terminal helix

connection linkers pack tightly to form a knot-like structure on the top of CH2 (Fig. 4i). Deletion of the C-terminal half of CH2 (905–931) did not dramatically affect hTRPC6 assembly and gating (Supplementary information, Figure S5 and Table S1) but further deletion of the entire CH2 and CH1–CH2 linker (878–931) greatly impaired tetrameric channel assembly, as shown by the dominant lower molecular weight peak on fluorescence-detection size-exclusion chromatography (FSEC) (Supplementary information, Figure S5a), indicating the essential role of the CH1–CH2 linker knot and the first half of the CH2 in tetramer assembly.

Transmembrane domain of the hTRPC6 channel

In the TMD, the voltage sensor-like domains (VSLDs, S1–S4) dock onto the four-fold symmetric ion channel pore (S5–S6) in a domain-swapped fashion, as evidenced by the strong density of S4–S5 linker (Fig. 5 and Supplementary information, Figure S3d). This is similar to other TRP channels.[33–40] It is worth noting that the S3 helix of hTRPC6 is longer than that of other TRP channels for about three turns in the extracellular C-terminus. Together with extracellular loops that connect transmembrane helices, the S3 C-terminus creates a distinctive large protrusion from TMD into the extracellular space (Fig. 2a–c). Among all of the available TRP channel structures, the TMD of hTRPC6 mostly resembles that of NOMPC[37] and TRPM,[29–32] as they share common structural elements of the pre-S1 elbow and the TRP re-entrant located after the TRP helix. According to the sequence alignments, these structural elements are also preserved in the Drosophila TRP channel and other mammalian TRPC channels (Supplementary information, Figure S4). The pore helix and pore loop interact extensively with S5–S6 gating helices (Supplementary information, Figure S7a-c), which might provide the structural basis for coupling between the gate and the selectivity filter observed experimentally in TRPC3.[41] The calculated pore profile showed that the radius of the narrowest constriction is 0.96 Å, which is smaller than that of dehydrated sodium ions (Fig. 5c). Therefore, the pore in the hTRPC6 structure is in a closed state. This is consistent with the fact that the high-affinity inhibitor BTDM was supplemented in our cryo-EM sample preparation. The polar residues N728 and Q732 and hydrophobic residue I724 line the narrowest constriction and form the gate on the intracellular side (Fig. 5c). On the extracellular side, the negatively charged E687 sits on top of the selectivity filter (Fig. 5c–e). It has been reported that the same residue on TRPC3 (E630 of TRPC3) governs divalent permeability,[41] consistent with its crucial position in our structure model. The conformation of hTRPC6 selectivity filter is similar to that of TRPM4[29–32] (Supplementary information, Figure S7d and e). In contrast, hTRPC6 is permeable to calcium ions while TRPM4 is not. This is because the crucial residue Q973 that governs ion permeability in TRPM4[29] is replaced by a leucine in hTRPC6 (Supplementary information, Figure S7d and e).

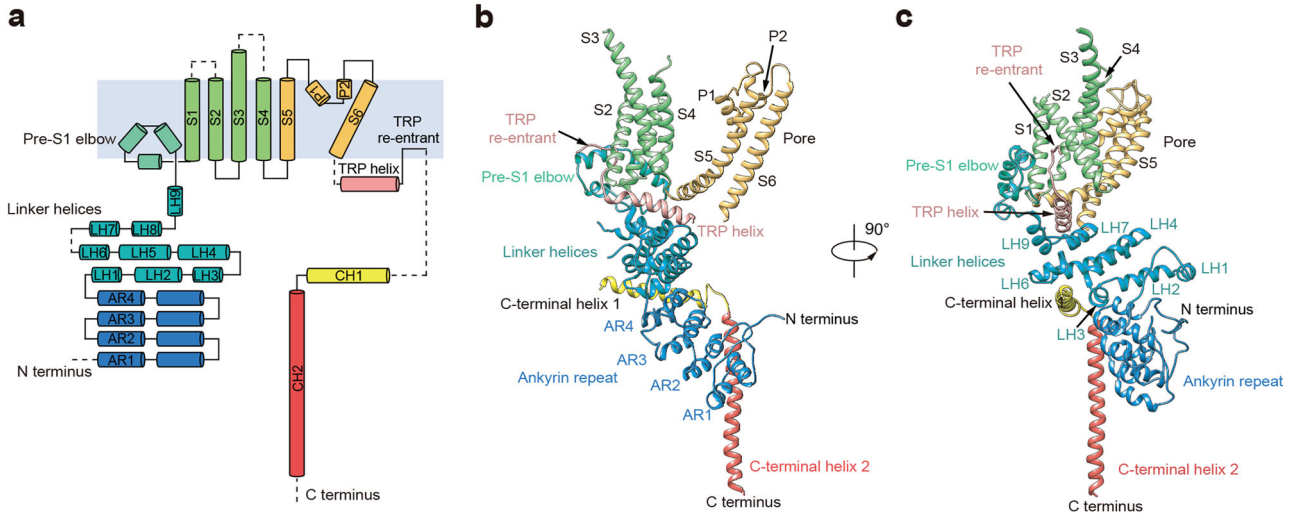

Fig. 3 Structure of a single TRPC6 subunit. **a** Topology and domain organization of hTRPC6. α-Helices are shown as cylinders. Dashed lines represent flexible regions with insufficient density for model building. **b**, **c** Ribbon diagrams show two views of one TRPC6 subunit with the same color as in **a**

TRP domain of the hTRPC6 channel

The TRP helix is sandwiched between the cytosolic LHs and the TMD (Fig. 6a). The LH7, LH8, and LH9 form a hydrophobic pocket to accommodate the bulky side chains of F744, W750, F751, and F754 on the cytosolic face of the TRP helix (Fig. 6b). On the membrane face of the TRP helix, W742, L749, and Y753 tightly pack against S1, S4, and S4–S5 linker of the TMD (Fig. 6c). The TRP re-entrant interacts with both the pre-S1 elbow and the S1 helix (Fig. 6d). Similar re-entering loop was also observed in the structures of NOMPC channel[37] and TRPM channel.[29–32] It has been reported that the conserved site ^{755}EE^{756} located between the TRP helix and the TRP re-entrant plays an important role in the STIM1-mediated gating of TRPC channels,[42] consistent with their crucial position observed in our structure (Fig. 6d).

The inhibitor BTDM-binding site

We found two extra densities in the map of the hTRPC6 TMD. One elongated extra density is surrounded by the pre-S1 elbow, S1, S4, and S4–S5 linker from one subunit and S5 from the adjacent subunit (Supplementary information, Figure S6a). To determine whether the surrounding residues might be involved in BTDM binding, we generated mutations of Y392F on the linker helix; A404C, F407A, L408M, and L411F on the pre-S1elbow; A447T, A447F, T451F, and T451L on S1; and N617S and F620L on the S4–S5 linker (Supplementary information, Figure S6a). These mutations did not markedly affect OAG-mediated channel activation and BTDM efficacy (Supplementary information, Table S1). Notably, in the TRPM4 structure,[43] a cholesteryl hemisuccinate (CHS) molecule occupies the similar position (Supplementary information, Figure S6b). Therefore, we speculate that this density corresponds to a CHS molecule used in protein purification. The other extra density in the hTRPC6 TMD is surrounded by S3, S4, and S4–S5 linker of one subunit and S5–S6 of the adjacent subunit (Fig. 7 and Supplementary information, Figure S6d). The position of this density is similar to the resiniferatoxin- and the capsaicin-binding site on TRPV1[44] (Supplementary information, Figure S6e). Residues W526 on S3, S608 on S4, Q624 and L627 on the S4–S5 linker from one subunit, together with residues I640 and V644 on S5, and T714 on S6 from the adjacent subunit create the binding pocket for the ligand represented by the extra density (Fig. 7b, c). We examined whether these residues are involved in BTDM binding by mutagenesis. We found that W526A and I640F had modest effects on BTDM function, whereas T714F and Q624A dramatically reduced BTDM affinity (Supplementary information, Table S1). Strikingly, BTDM had little effect on S608L and V644F mutants, even at 10 μM concentration (Supplementary information, Table S1). These mutants had normal OAG activation but impaired BTDM inhibition (Supplementary information, Table S1), emphasizing the importance of these residues in BTDM binding and suggesting that this pocket with extra density bound inside might represent the BTDM-binding site on hTRPC6 channel. Residues involved in BTDM binding are conserved between hTRPC3 and hTRPC6 (Supplementary information, Figure S4), consistent with the fact that BTDM is potent toward both hTRPC3 and hTRPC6 (Supplementary information, Figure S1b-e). However, BTDM is a molecule with many possible rotamer conformations and limited local map quality precluded accurate modeling of BTDM into the extra density. Thus the detailed binding mode of BTDM needs further investigation.

Structure of the hTRPC3 channel

During the cryo-EM sample preparation for the hTRPC3 channel, we supplemented the lipid-activator OAG instead of the inhibitor BTDM into the nanodisc sample. The final cryo-EM map of the hTRPC3 channel at 4.4 Å resolution shows a similar structure as hTRPC6, consistent with their high sequence homology (73% identity) and emphasizing the structural conservation of receptor-activated TRPC family channels (Supplementary information, Figures S4 and S8). The ion channel pore of hTRPC3 is also in the closed state, essentially the same as that of hTRPC6. We found that the BTDM-binding site in the cryo-EM map of hTRPC3 is devoid of strong density (Supplementary information, Figure S6f). In contrast, the CHS density persists (Supplementary information, Figure S6c), further validating our former assignment of the BTDM density. In the hTRPC3 map, we did not observe strong extra densities that might correspond to OAG molecules we added into the sample, probably due to its low-binding affinity (Supplementary information, Figure S1d). By comparing the structures of hTRPC6 and hTRPC3 at the BTDM-binding site in TMD, we observed a relatively small but noticeable movement between VSLDs and the S5–S6 pore. With the S6-TRP domain linker as the hinge, the VSLD of BTDM-bound TRPC6 rotates as a rigid body toward the pore. This results in a 1° rotation between the S3

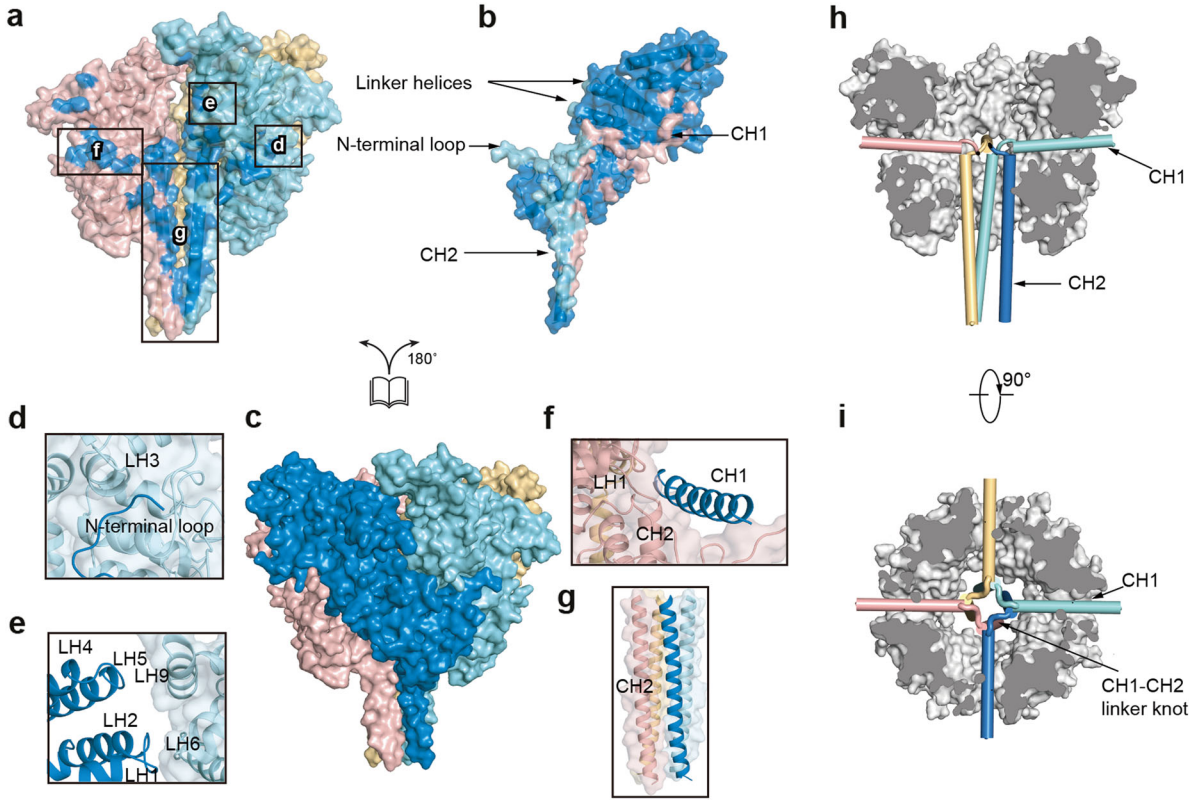

Fig. 4 Inter-subunit interface of hTRPC6 ICD. **a**–**c** Open-book view of hTRPC6 ICD inter-subunit interface shown in surface representation. Surface of each subunit is in transparency and colored the same as in Fig. 2. View of the ICDs of subunits A, C, and D is shown in **a** and residues that interact with the subunit B are colored in blue. View of the ICD of subunit B is shown in **b** and residues that interact with subunits A, C, and D are colored in cyan, pink, and yellow, respectively. View of the ICD layer tetramer is shown in **c**. **d**–**g** Close-up view of the inter-subunit interactions boxed in **a**. **h** Side view of CH1 and CH2 locations. CH1 and CH2 are shown as cylinders and colored the same as in **c**. The other parts of ICD are colored in gray. CH2 of subunit C and CH1 of subunit B are omitted for better illustration. **i** Top view of CH1 and CH2 locations.

helices and 1.7 Å displacement of Y500 Cα atom (Fig. 8a). We also found that the ICD of hTRPC6 has a 3° clockwise rotation relative to that of hTRPC3 when the TMD is aligned (Fig. 8b). These subtle conformational differences might be due to BTDM binding in the hTRPC6 structure and the structural variation between the TRPC3 and TRPC6 channel subtypes.

DISCUSSION

The structures of hTRPC6 and hTRPC3 presented here provide a view of the architecture of this receptor-activated TRPC channel family. The large ICD harbors important sites for modulatory protein binding[24–26] and upstream kinase phosphorylation.[45] It acts as an antenna to sense these intracellular signals and talks to the TMD via the TRP domain that bridges ICD and TMD. The TRPC TMD harbors not only the cation permeation pathway but also the site for ligand binding. The high-affinity inhibitor BTDM wedges between the VSLD and the pore to inhibit channel gating. Our structures not only provide a template for structure-based drug discovery for hTRPC6 but also pave the way to a better understanding of the gating mechanism of receptor-activated TRPC family channels.

MATERIALS AND METHODS

Cell culture

Sf9 cells were cultured in Sf-900 III serum-free medium (SFM; Thermo Fisher Scientific) at 27 °C. FreeStyle 293-F cells were cultured in FreeStyle 293 medium (Thermo Fisher Scientific) supplemented with 1% fetal bovine serum (FBS) at 37 °C with 6% CO_2 and 70% humidity.

Electrophysiology

hTRPC6 channel activation was measured using the whole-cell patch-clamp technique. OAG 10 μM was used to activate current in hTRPC6 stable expressing cells (TRPC6-HEK293, PerkinElmer Company). Cells were placed in a small chamber and continuously perfused with an external solution (~3 ml/min) using a RSC-200 perfusion system (Science Instruments, BioLogic). All current recordings were conducted at room temperature (~22 °C). Electrodes were made from glass capillary tubes and had a resistance of 2–4 MΩ when filled with one of the internal solutions. For hTRPC6 current recording, the intracellular solution contains (in mM): 120 CsOH, 120 Aspartate, 20 CsCl, 2 $MgCl_2$, 0.4 $CaCl_2$, 10 HEPES, 2 Na_2ATP, 0.1 Na_3GTP, 10 Glucose, and 1 EGTA (pH 7.2–7.25, adjusted with CsOH). The extracellular solution contains (in mM): 145 NaCl, 5 KCl, 1 $CaCl_2$, 1 $MgCl_2$, 10 HEPES, and 10 Glucose (pH 7.4 adjusted with NaOH). After whole-cell configuration was established, cell membrane capacitance was canceled electronically and the series resistance was compensated by about 70%. TRPC6 current was induced by a 300 ms voltage ramp protocol (from +100 mV to −100 mV) every 10 s at a holding potential of −60 mV. Once the control current is stabilized, the recording chamber is perfused with external solution containing testing compound. The TRPC6 current is measured as the average current at +100 mV. The time course of current is plotted for the

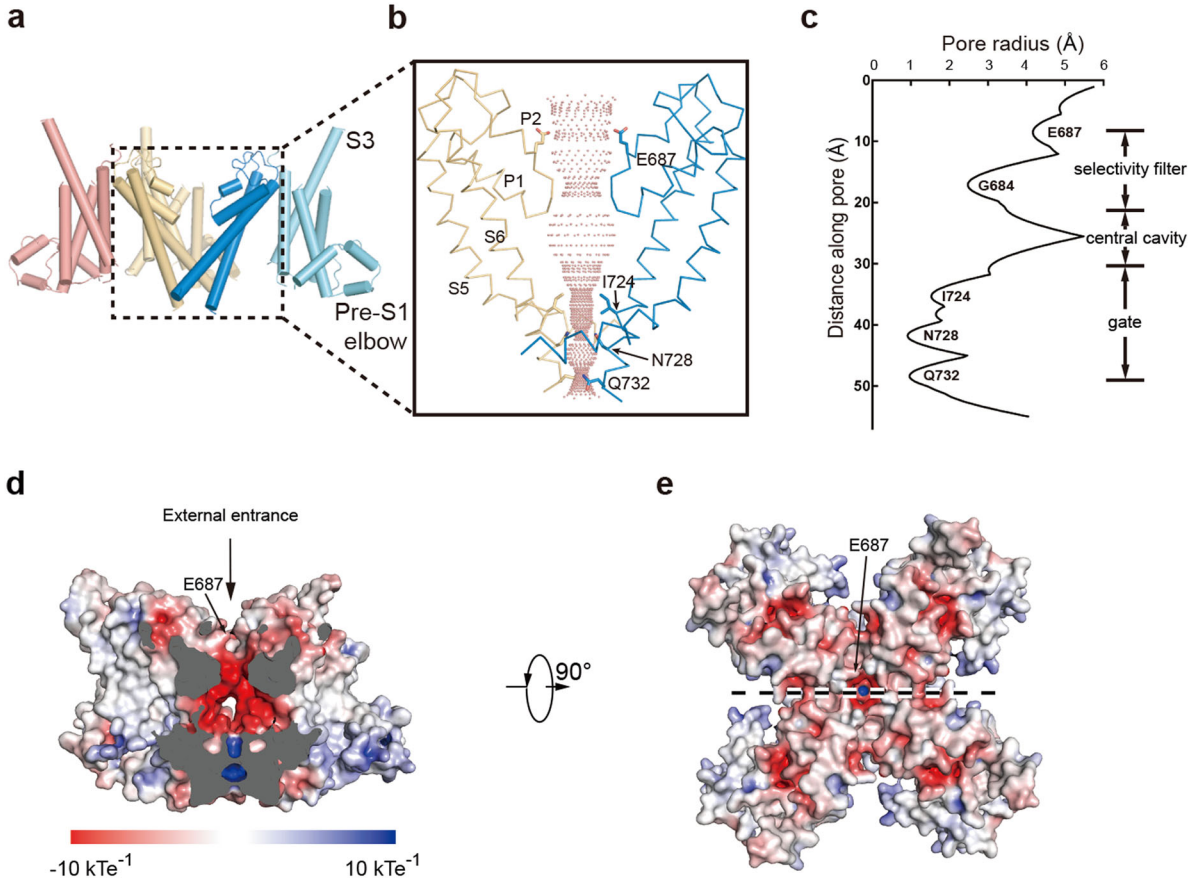

Fig. 5 Structure of the hTRPC6 TMD. **a** Side view of the hTRPC6 TMD in cartoon representation. S5–S6 of the subunits B and D and S1–S4 of the subunit C are omitted for better illustration. **b** Close-up view of the S5–S6 pore region boxed in **a**. Ion-permeation pathway along the pore was calculated with the HOLE program. **c** Calculated pore radius corresponding to **b** is shown vertically. **d** Central cross-section of hTRPC6 transmembrane domain shown as surface and colored by electrostatic potential. Arrow indicates the external ion entrance. Position of E687 on top of the selectivity filter is indicated by an arrow. **e** Top view of hTRPC6 transmembrane domain. A dashed line in **e** indicates the position of central cross-section in **d**

whole experiment. Percent inhibition $= 100 \times (1 - I_D/I_c)$, where I_D is the current amplitude measured at the end of a particular drug concentration and I_c is the control current amplitude measured before drug application. Zero current (background) level was set at the very beginning before OAG-activated TRPC6 current. Whole-cell currents of hTRPC3 were measured in a similar way as hTRPC6, except using a home-made TRPC3-AD293 stable cell line and the intracellular solution containing (in mM):130 CsCl, 5 HEPES, 5 EGTA, 5 Na_2ATP, 0.1 Na_3GTP, and 5.5 $MgCl_2$ (pH 7.2–7.25, adjusted with CsOH). The extracellular solution contained (in mM): 140 NaCl, 4 KCl, 1 $MgCl_2$, 10 HEPES, 0.2 $CaCl_2$, 10 Glucose, and 2 Na_4EDTA (pH 7.4 adjusted with NaOH). MultiClamp 700B amplifier with Digidata 1440 interface and pCLAMP software (AXON Instruments) were used for data acquisition and analysis. All the reagents are purchased from Sigma Company.

FSEC

The cDNA of hTRPC6 was cloned into a home-made N-terminal green fluorescent protein (GFP)-tagged BacMam vector.[46] Various hTRPC6 constructs were screened by transfecting vectors into FreeStyle 293-F cells (Thermo Fisher Scientific, grown in 293Ti medium, 37 °C). Cells were harvested 48 h post-transfection and solubilized in Tris buffered saline (TBS; 20 mM Tris pH 8.0 at 4 °C, 150 mM NaCl) with 10 mM lauryl maltose-neopentyl glycol (LMNG; Anatrace), 0.1% CHS (Anatrace), and protease inhibitors including 1 μg/ml aprotinin, 1 μg/ml leupeptin, and 1 μg/ml pepstatin on ice for 30 min. Cell lysates were cleared by centrifuge at 40,000 rpm for 30 min and supernatants were loaded onto Superose 6 increase (GE Healthcare) for FSEC analysis.[47]

FLIPR membrane potential assay

hTRPC6 and hTRPC3 constructs were transfected into AD 293 cells (grown in Dulbecco's Modified Eagle's Medium + 10% FBS, 37 °C) and seeded on 384-well plates at the density of ~10,000 cells/well for FLIPR assay using FLIPR Membrane Potential Assay Reagent (Thermo Fisher). For the inhibition curves, OAG was added to 10 μM final concentration for TRPC6 and 2 μM final concentration for TRPC3. Fluorescence signals were read with excitation/emission at 510–545/565–625 nm. EC_{50} was obtained by fitting the data into the function: $Y = \text{Bottom} + (\text{Top–Bottom})/(1 + 10^{(\text{LogEC50}-X)})$ and IC_{50} was obtained by fitting the data into function: $Y = \text{Bottom} + (\text{Top–Bottom})/(1 + 10^{(X-\text{LogIC50})})$.

Protein expression and purification

We established the BacMam expression system for large-scale expression of full-length hTRPC6 as describe before.[46] Briefly, full-length hTRPC3 or hTRPC6 was subcloned into a home-made BacMam vector with N terminal strep-GFP tag. Bacmid was then generated by transforming this construct into DH10Bac *Escherichia coli* cells. Baculovirus was harvested about 1 week after transfecting bacmid into Sf9 cells cultured in Sf-900 III SFM medium (Gibco) at 27 °C. When FreeStyle 293-F cells (grown in FreeStyle 293 medium + 1% FBS, 37 °C) in suspension were grown to a density of 2.0×10^6/ml, baculovirus was added to it. Twelve hours after

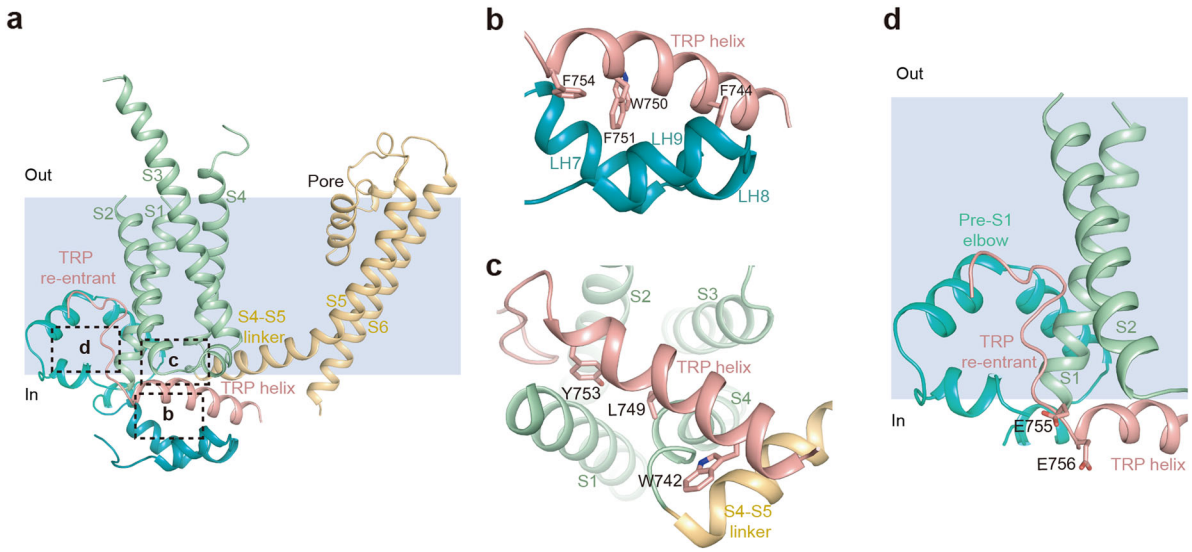

Fig. 6 TRP domain of hTRPC6. **a** Side view of LHs and TMD of one hTRPC6 subunit. Each structure element is colored the same as in Fig. 3. Position of putative membrane bilayer is shown in light blue. **b** Close-up view of interactions between TRP helix and LHs, boxed in **a**. **c** Bottom view of the interactions between TRP helix and VSLD, boxed in **a**. **d** Close-up view of the TRP re-entrant boxed in **a**

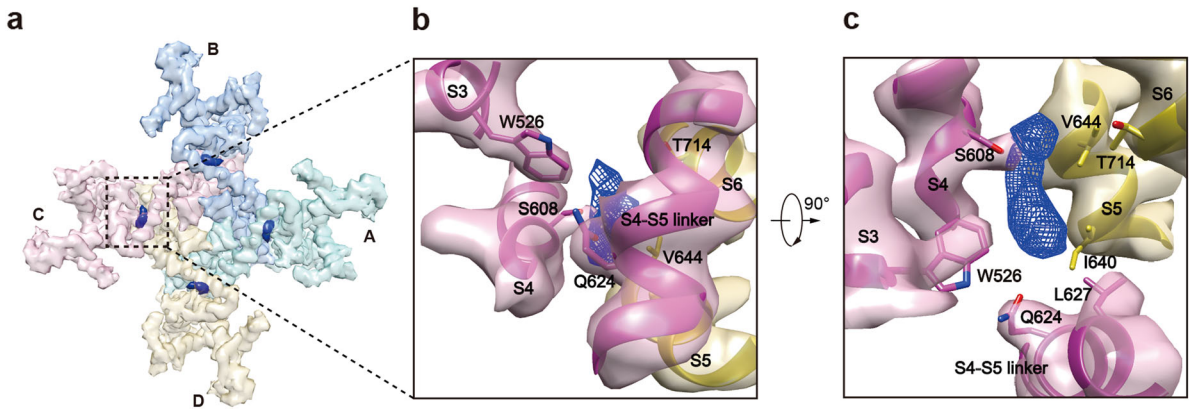

Fig. 7 BTDM densities observed in hTRPC6 structure. **a** Cryo-EM density map of hTRPC6 transmembrane domain from bottom view. Each subunit is colored the same as in Fig. 2. Protein density is in transparency. BTDM density is colored in blue. **b**, **c** Close-up view of BTDM-binding site from bottom and side views

infection, 10 mM sodium butyrate and 100 nM BTDM were added and temperature was lowered to 30 °C. Cells were harvested 60 h postinfection and washed twice using TBS buffer (20 mM Tris pH 8.0 at 4 °C, 150 mM NaCl). Cell pellets were frozen at −80 °C for use.

Cell pellets were resuspended in TBS buffer containing 10 mM LMNG, 0.1% CHS, 100 nM BTDM, and protease inhibitors, including 1 μg/ml aprotinin, 1 μg/ml leupeptin, 1 μg/ml pepstatin, and 1 mM phenylmethanesulfonylfluoride and rotated at 4 °C for 1 h. Unbroken cells and large cell debris were removed by centrifugation at 14,800 rpm for 10 min. Supernatants were further centrifuged at 40,000 rpm for 40 min in Ti45 rotor (Beckman). After centrifugation, appropriate amount of purified glutathione *S*-transferase-tagged GFP-nanobody[48] was added to the supernatant and rotated at 4 °C for 10 min. Then samples were loaded on 7 ml GS4B resin (GE Healthcare). Resin was washed with wash buffer 1 (TBS + 40 μM glyco-diosgenin (GDN) + 0.01 mg/ml soybean lipids + 100 nM BTDM). Then it was further washed with wash buffer 2 (wash buffer 1 + 10 mM $MgCl_2$ + 1 mM ATP) to remove bound chaperones. Protein was eluted with elution buffer (10 mM reduced glutathione + 50 mM Tris (pH 8.0 at room temperature) + 40 μM GDN + 0.01 mg/ml soybean lipids + 100 nM BTDM + 4 mM dithiothreitol) and concentrated using 100-kDa cut-off concentrator (Millipore). To cleave the tags off the hTRPC6 protein and remove glycosylation, concentrated proteins were incubated with H3CV protease and PNGase F at 4 °C overnight. Proteins were further purified by Superose 6 increase (GE Healthcare) running in buffer containing TBS, 40 μM GDN, 0.01 mg/ml soybean lipids, 100 nM BTDM, and 1 mM Tris (2-carboxyethyl) phosphine (TCEP). The peak fractions corresponding to tetrameric TRPC channel were collected, concentrated, and mixed with soybean lipids and purified MSP2N2 (prepared as described previously[49]) at a molar ratio of TRPC6 monomer: MSP2N2:soybean lipids = 1:7:225 to initiate nanodisc reconstitution. After incubating the mixture at 4 °C for 30 min, Bio-beads SM2 (Bio-Rad) were added and the reconstitution system was rotated at 4 °C for 1 h before another batch of fresh bio-beads were added. The system was rotated at 4 °C overnight. Bio-beads were removed and the reconstitution system were cleared by centrifugation at 40,000 rpm for 30 min before loaded onto a Superose-6 increase column running in TBS containing 1 mM TCEP. The peak fractions corresponding to tetrameric hTRPC6 channel in nanodiscs were assessed by sodium dodecyl sulfate-polyacrylamide gel electrophoresis. hTRPC3 channel protein was purified in the same way as hTRPC6.

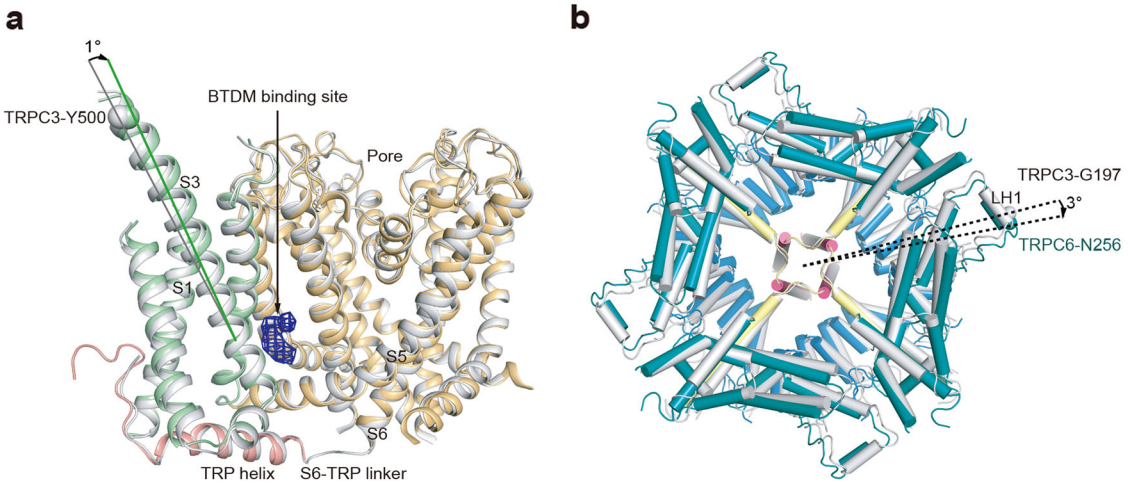

Fig. 8 Structural comparison between hTRPC3 and hTRPC6 in allosterically inhibited state. **a** Comparison of the TRPC TMD structures. S5–S6 of one subunit are aligned. hTRPC3 is in gray and hTRPC6 is colored the same as in Fig. 3. Only one copy of S1–S4 and TRP domain is shown for better visualization. Angle between S3 helices of the two structures is labeled. Cα position of hTRPC3 Y500 is shown as sphere. The BTDM density is colored in blue. **b** Comparison of the TRPC ICD structures. The TMD of hTRPC3 and hTRPC6 structures are aligned. hTRPC3 is in gray and hTRPC6 is colored the same as in Fig. 3. The angle between ICDs is measured using Cα positions of N256 of hTRPC6 (shown as blue sphere) and G197 of hTRPC3 (shown as gray sphere)

EM sample preparation

Purified hTRPC6 nanodisc was concentrated to A280 = 4.5 with estimated concentration of 35.8 μM monomers and supplemented with 100 μM BTDM. To overcome the preferred orientation of particles in ice, 0.5 mM non-solubilizing detergent fluorinated octyl-maltoside[50] was added to the sample before cyro-EM sample preparation. Protein samples were loaded onto glow-discharged GiG R1/1 holey carbon grids and plunged into liquid ethane by Vitrobot Mark IV (Thermo Fisher) at the Institute of Biophysics, Chinese Academy of Sciences. hTRPC3 samples were prepared in a similar procedure except that OAG was added to 380 μM final concentration.

Data collection

The cryo-grids were first screened on a Talos (Thermo Fisher) operated at a voltage of 200 kV with an eagle 4k × 4k CCD camera (Thermo Fisher). For hTRPC6 data collection, grids were imaged with a GatanK2 Summit direct detector camera on Titan Krios (Thermo Fisher) at the National Center for Protein Science Shanghai at the voltage of 300 kV, with a Cs corrector, magnification of 37,500×, equivalently to the pixel size of 1.33 Å, and with defocus values ranging from −1.0 to −3.0 μm. Super-resolution movies (50 frames per movie) acquisition were performed automatically using Serial EM[51] with a dose rate of 8 e^-/pixel/s on detector and a total dose 50 $e^-/Å^2$. hTRPC3 data were collected in a similar way except on a Titan Krios microscope in Peking University without Cs corrector. Super-resolution movies (50 frames per movie) were collected with a dose rate of 6.7 e^-/pixel/s on a K2 detector mounted after an energy filter with 20 eV slit.

Image processing

For hTRPC6, 1868 movies were collected. MotionCor2[52] was used for image binning, motion correction and dose weighting. After motion correction, about 120 bad micrographs were removed. GCTF[53] was used for CTF estimation of all the motion-corrected sums (1748 movies). After manual picking particles, reference-free two-dimensional (2D) classification was performed using Relion2.0.[54] The resulting 2D averages were used as templates for autopicking on all micrographs. Repeated 2D classification was used to remove bad particles, leaving 189,781 particles for three-dimensional (3D) classification. An ab initio 3D reconstruction was generated using cryoSPARC.[55] This initial model was used as the initial reference for 3D classification in Relion2.0 without any symmetry restrains. After 3D classification, one class containing 53,528 particles with clearly visible α helices was selected for 3D refinements in cryoSPARC using C4 symmetry. The reconstruction reaches 3.8 Å, based on gold standard FSC 0.143 cut-off after correction of masking effect.[56] The map was sharpened with a *B*-factor of $-166.8\ Å^2$ determined by cryoSPARC automatically. The data processing of hTRPC3 follows the same protocol and is detailed in Supplementary information, Table S2.

Model building

Ab initio model of hTRPC6 was built using EM builder[55] and Rosetta CM.[57] The model was further manually rebuilt using Coot,[58] using the structure of NOMPC (5VKQ) as reference of TMD. Structure was refined with PHENIX[59] against sharpened map. Pore radius was calculated with HOLE.[60] The model of hTRPC3 was obtained by homology modeling using SWISS-MODEL[61] with hTRPC6 as reference. The model was fitted into the map of hTRPC3, manually rebuilt and refined by PHENIX.[59]

Quantification and statistical analysis

The orientation distribution of the particles used in the final reconstruction was calculated using RELION 2.0. The local resolution map was calculated using ResMap.[62]

Data availability

3D cryo-EM density map of hTRPC6 has been deposited to the Electron Microscopy Data Bank (EMDB) under the accession number: EMD-6856. Coordinates of atomic model of hTRPC6 has been deposited in the Protein Data Bank (PDB) under the accession number: 5YX9. 3D cryo-EM density map of hTRPC3 has been deposited to the EMDB under the accession number: EMD-6911. Coordinates of atomic model of hTRPC3 has been deposited in the PDB under the accession number: 5ZBG. All other data are available from the corresponding authors upon reasonable request.

ACKNOWLEDGEMENTS

We thank all of Chen Laboratory members for their kind help. Cryo-EM data collection was supported by the National Center for Protein Science (Shanghai) with assistance

of Liangliang Kong and Zhenglin Fu, Electron Microscopy Laboratory and Cryo-EM platform of Peking University with assistance of Xuemei Li and Daqi Yu, and Center for Biological Imaging, Institute of Biophysics, Chinese Academy of Science with assistance of Zhenxi Guo. Part of structural computation was also performed on the Computing Platform of the Center for Life Science and High-performance Computing Platform of Peking University. The work is supported by grants from the Ministry of Science and Technology of China (National Key R&D Program of China, 2016YFA0502004 to L.C.), National Natural Science Foundation of China (31622021 and 31521062 to L.C.), Young Thousand Talents Program of China to L.C. and the China Postdoctoral Science Foundation (2016M600856 and 2017T100014 to J.-X.W.). J.-X.W. is supported by the postdoctoral foundation of the Peking-Tsinghua Center for Life Sciences, Peking University.

AUTHOR CONTRIBUTIONS

X. Zhang and L.C. initiated the project. Q.T., W.G., L.Z., M.L., X. Zhou, X. Zhang, and L.C. designed the experiments. Q.T., W.G., J.-X.W., and L.C. prepared the EM sample, collected the EM data, performed image processing, and built the model. Q.T. and W.G. generated mutants. L.Z., M.L., X. Zhou, and X. Zhang provided BTDM and performed electrophysiology recording and FLIPR assay. Q.T., W.G., J.-X.W., and L.C. wrote the manuscript draft. All authors contributed to manuscript preparation.

ADDITIONAL INFORMATION

Supplementary information accompanies this paper at https://doi.org/10.1038/s41422-018-0038-2.

Competing interests: L.Z., M.L., X. Zhou and X. Zhang are employees of Dizal Pharmaceutical Company. The other authors declare no competing interests.

REFERENCES

1. Montell, C. & Rubin, G. M. Molecular characterization of the Drosophila trp locus: a putative integral membrane protein required for phototransduction. *Neuron* **2**, 1313–1323 (1989).
2. Hardie, R. C. & Minke, B. The trp gene is essential for a light-activated Ca2+channel in Drosophila photoreceptors. *Neuron* **8**, 643–651 (1992).
3. Li, H. TRP channel classification. *Adv. Exp. Med. Biol.* **976**, 1–8 (2017).
4. Hofmann, T. et al. Direct activation of human TRPC6 and TRPC3 channels by diacylglycerol. *Nature* **397**, 259–263 (1999).
5. Okada, T. et al. Molecular and functional characterization of a novel mouse transient receptor potential protein homologue TRP7. Ca(2+)-permeable cation channel that is constitutively activated and enhanced by stimulation of G protein-coupled receptor. *J. Biol. Chem.* **274**, 27359–27370 (1999).
6. Trebak, M., Vazquez, G., Bird, G. S. & Putney, J. W. Jr. The TRPC3/6/7 subfamily of cation channels. *Cell Calcium* **33**, 451–461 (2003).
7. Hofmann, T., Schaefer, M., Schultz, G. & Gudermann, T. Subunit composition of mammalian transient receptor potential channels in living cells. *Proc. Natl. Acad. Sci. USA* **99**, 7461–7466 (2002).
8. Zhou, J. et al. Critical role of TRPC6 channels in the formation of excitatory synapses. *Nat. Neurosci.* **11**, 741–743 (2008).
9. Hartmann, J. et al. TRPC3 channels are required for synaptic transmission and motor coordination. *Neuron* **59**, 392–398 (2008).
10. Reiser, J. et al. TRPC6 is a glomerular slit diaphragm-associated channel required for normal renal function. *Nat. Genet.* **37**, 739–744 (2005).
11. Winn, M. P. et al. A mutation in the TRPC6 cation channel causes familial focal segmental glomerulosclerosis. *Science* **308**, 1801–1804 (2005).
12. Davis, J., Burr, A. R., Davis, G. F., Birnbaumer, L. & Molkentin, J. D. A TRPC6-dependent pathway for myofibroblast transdifferentiation and wound healing in vivo. *Dev. Cell* **23**, 705–715 (2012).
13. Yang, S. L., Cao, Q., Zhou, K. C., Feng, Y. J. & Wang, Y. Z. Transient receptor potential channel C3 contributes to the progression of human ovarian cancer. *Oncogene* **28**, 1320–1328 (2009).
14. Tsvilovskyy, V. V. et al. Deletion of TRPC4 and TRPC6 in mice impairs smooth muscle contraction and intestinal motility in vivo. *Gastroenterology* **137**, 1415–1424 (2009).
15. Onohara, N. et al. TRPC3 and TRPC6 are essential for angiotensin II-induced cardiac hypertrophy. *EMBO J.* **25**, 5305–5316 (2006).
16. Heeringa, S. F. et al. A novel TRPC6 mutation that causes childhood FSGS. *PLoS ONE* **4**, e7771 (2009).
17. Zhu, B. et al. Identification and functional analysis of a novel TRPC6 mutation associated with late onset familial focal segmental glomerulosclerosis in Chinese patients. *Mutat. Res.* **664**, 84–90 (2009).
18. Gigante, M. et al. TRPC6 mutations in children with steroid-resistant nephrotic syndrome and atypical phenotype. *Clin. J. Am. Soc. Nephrol.* **6**, 1626–1634 (2011).
19. D'Agati, V. D., Kaskel, F. J. & Falk, R. J. Focal segmental glomerulosclerosis. *N. Engl. J. Med.* **365**, 2398–2411 (2011).
20. Ilatovskaya, D. V. & Staruschenko, A. TRPC6 channel as an emerging determinant of the podocyte injury susceptibility in kidney diseases. *Am. J. Physiol. Ren. Physiol.* **309**, F393–397 (2015).
21. Beer, A., Mayer, G. & Kronbichler, A. Treatment strategies of adult primary focal segmental glomerulosclerosis: a systematic review focusing on the last two decades. *Biomed. Res. Int.* **2016**, 4192578 (2016).
22. Dragovic, D. et al. Increasing incidence of focal segmental glomerulosclerosis and an examination of demographic patterns. *Clin. Nephrol.* **63**, 1–7 (2005).
23. Fogo, A. B. Causes and pathogenesis of focal segmental glomerulosclerosis. *Nat. Rev. Nephrol.* **11**, 76–87 (2015).
24. Kwon, Y., Hofmann, T. & Montell, C. Integration of phosphoinositide- and calmodulin-mediated regulation of TRPC6. *Mol. Cell* **25**, 491–503 (2007).
25. Boulay, G. Ca(2+)-calmodulin regulates receptor-operated Ca(2+) entry activity of TRPC6 in HEK-293 cells. *Cell Calcium* **32**, 201–207 (2002).
26. Zhang, Z. Activation of Trp3 by inositol 1,4,5-trisphosphate receptors through displacement of inhibitory calmodulin from a common binding domain. *Proc. Natl. Acad. Sci. USA* **98**, 3168–3173 (2001).
27. Lepage, P. K. et al. Identification of two domains involved in the assembly of transient receptor potential canonical channels. *J. Biol. Chem.* **281**, 30356–30364 (2006).
28. Paulsen, C. E., Armache, J. P., Gao, Y., Cheng, Y. & Julius, D. Structure of the TRPA1 ion channel suggests regulatory mechanisms. *Nature* **525**, 552 (2015).
29. Guo, J. et al. Structures of the calcium-activated, non-selective cation channel TRPM4. *Nature* https://doi.org/10.1038/nature24997 (2017).
30. Winkler, P. A., Huang, Y., Sun, W., Du, J. & Lu, W. Electron cryo-microscopy structure of a human TRPM4 channel. *Nature* https://doi.org/10.1038/nature24674 (2017).
31. Autzen, H. E. et al. Structure of the human TRPM4 ion channel in a lipid nanodisc. *Science* https://doi.org/10.1126/science.aar4510 (2017).
32. Yin, Y. et al. Structure of the cold- and menthol-sensing ion channel TRPM8. *Science* https://doi.org/10.1126/science.aan4325 (2017).
33. Liao, M., Cao, E., Julius, D. & Cheng, Y. Structure of the TRPV1 ion channel determined by electron cryo-microscopy. *Nature* **504**, 107–112 (2013).
34. Huynh, K. W. et al. Structure of the full-length TRPV2 channel by cryo-EM. *Nat. Commun.* **7**, 11130 (2016).
35. Zubcevic, L. et al. Cryo-electron microscopy structure of the TRPV2 ion channel. *Nat. Struct. Mol. Biol.* **23**, 180–186 (2016).
36. Shen, P. S. et al. The structure of the polycystic kidney disease channel PKD2 in lipid nanodiscs. *Cell* **167**, 763–773 e711 (2016).
37. Jin, P. et al. Electron cryo-microscopy structure of the mechanotransduction channel NOMPC. *Nature* **547**, 118–122 (2017).
38. Chen, Q. et al. Structure of mammalian endolysosomal TRPML1 channel in nanodiscs. *Nature* **550**, 415–418 (2017).
39. Hirschi, M. et al. Cryo-electron microscopy structure of the lysosomal calcium-permeable channel TRPML3. *Nature* **550**, 411–414 (2017).
40. Schmiege, P., Fine, M., Blobel, G. & Li, X. Human TRPML1 channel structures in open and closed conformations. *Nature* **550**, 366–370 (2017).
41. Lichtenegger, M. et al. A novel homology model of TRPC3 reveals allosteric coupling between gate and selectivity filter. *Cell Calcium* **54**, 175–185 (2013).
42. Zeng, W. et al. STIM1 gates TRPC channels, but not Orai1, by electrostatic interaction. *Mol. Cell.* **32**, 439–448 (2008).
43. Autzen, H. E. et al. Structure of the human TRPM4 ion channel in a lipid nanodisc. *Science* **359**, 228–232 (2018).
44. Cao, E., Liao, M., Cheng, Y. & Julius, D. TRPV1 structures in distinct conformations reveal activation mechanisms. *Nature* **504**, 113–118 (2013).
45. Voolstra, O. & Huber, A. Post-translational modifications of TRP channels. *Cells* **3**, 258–287 (2014).
46. Goehring, A. et al. Screening and large-scale expression of membrane proteins in mammalian cells for structural studies. *Nat. Protoc.* **9**, 2574–2585 (2014).
47. Kawate, T. & Gouaux, E. Fluorescence-detection size-exclusion chromatography for precrystallization screening of integral membrane proteins. *Structure* **14**, 673–681 (2006).
48. Kirchhofer, A. et al. Modulation of protein properties in living cells using nanobodies. *Nat. Struct. Mol. Biol.* **17**, 133–138 (2010).
49. Lynch, C. J. et al. Some cannabinoid receptor ligands and their distomers are direct-acting openers of SUR1 K(ATP) channels. *Am. J. Physiol. Endocrinol. Metab.* **302**, E540–551 (2012).
50. Efremov, R. G., Leitner, A., Aebersold, R. & Raunser, S. Architecture and conformational switch mechanism of the ryanodine receptor. *Nature* **517**, 39–43 (2015).
51. Mastronarde, D. N. Automated electron microscope tomography using robust prediction of specimen movements. *J. Struct. Biol.* **152**, 36–51 (2005).
52. Zheng, S. Q. et al. MotionCor2: anisotropic correction of beam-induced motion for improved cryo-electron microscopy. *Nat. Methods* **14**, 331–332 (2017).

53. Zhang, K. Gctf: real-time CTF determination and correction. *J. Struct. Biol.* **193**, 1–12 (2016).
54. Kimanius, D., Forsberg, B. O., Scheres, S. H. & Lindahl, E. Accelerated cryo-EM structure determination with parallelisation using GPUs in RELION-2. *eLife* **5**, e18722 (2016).
55. Zhou, N., Wang, H. & Wang, J. EMBuilder: a template matching-based automatic model-building program for high-resolution cryo-electron microscopy maps. *Sci. Rep.* **7**, 2664 (2017).
56. Chen, S. et al. High-resolution noise substitution to measure overfitting and validate resolution in 3D structure determination by single particle electron cryomicroscopy. *Ultramicroscopy* **135**, 24–35 (2013).
57. DiMaio, F. et al. Atomic-accuracy models from 4.5-A cryo-electron microscopy data with density-guided iterative local refinement. *Nat. Methods* **12**, 361–365 (2015).
58. Emsley, P., Lohkamp, B., Scott, W. G. & Cowtan, K. Features and development of Coot. *Acta Crystallogr. D Biol. Crystallogr.* **66**, 486–501 (2010).
59. Adams, P. D. et al. PHENIX: a comprehensive Python-based system for macromolecular structure solution. *Acta Crystallogr. D Biol. Crystallogr.* **66**, 213–221 (2010).
60. Smart, O. S., Neduvelil, J. G., Wang, X., Wallace, B. A. & Sansom, M. S. HOLE: a program for the analysis of the pore dimensions of ion channel structural models. *J. Mol. Graph.* **14**, 354–360 (1996). 376.
61. Biasini, M. et al. SWISS-MODEL: modelling protein tertiary and quaternary structure using evolutionary information. *Nucleic Acids Res.* **42**, W252–258 (2014).
62. Kucukelbir, A., Sigworth, F. J. & Tagare, H. D. Quantifying the local resolution of cryo-EM density maps. *Nat. Methods* **11**, 63–65 (2014).